Constraint-based Design of Parallel Kinematic XY Flexure Mechanisms

Shorya Awtar[1]
Precision Engineering Research Group
Massachusetts Institute of Technology, Cambridge MA
518-577-5500, shorya@mit.edu

Alexander H. Slocum
Professor of Mechanical Engineering, Precision Engineering Research Group
Massachusetts Institute of Technology, Cambridge MA
617-253-0012, slocum@mit.edu

Abstract

This paper presents parallel kinematic XY flexure mechanism designs based on systematic constraint patterns that allow large ranges of motion without causing over-constraint or significant error motions. Key performance characteristics of XY mechanisms such as mobility, cross-axis coupling, parasitic errors, actuator isolation, drive stiffness, lost motion, and geometric sensitivity are discussed. The standard double parallelogram flexure module is used as a constraint building-block and its non-linear force-displacement characteristics are employed in analytically predicting the performance characteristics of two proposed XY flexure mechanism designs. Fundamental performance tradeoffs, including those resulting from the non-linear load-stiffening and elastokinematic effects, in flexure mechanisms are highlighted. Comparisons between closed-form linear and non-linear analyses are presented to emphasize the inadequacy of the former. It is shown that geometric symmetry in the constraint arrangement relaxes some of the design tradeoffs, resulting in improved performance. The non-linear analytical predictions are validated by means of computational FEA and experimental measurements.

Keywords: Constraint-based Flexure Design, XY Flexure, Non-linear Flexure Analysis, Flexure Performance Characteristics, Flexure Design Tradeoffs, Center of Stiffness

---

[1] Corresponding Author

1. Introduction and Background

Compact XY flexure stages that provide large range of motion are desirable in several applications such as semiconductor mask and wafer alignments [1], scanning interferometry and atomic force microscopy [2-3], micromanipulation and microassembly [4], high-density memory storage [5], and MEMS sensors and actuators [6-7]. Despite numerous designs that exist in the technical literature [1, 8-10], flexure stages generally lack in motion range. Challenges in the design of large range mechanisms arise from the basic tradeoff between Degrees of Freedom (DOF) and Degrees of Constraint (DOC) in flexures [11]. As constraint elements, flexures pose a compromise between the motion range along DOF and the stiffness and error motions along DOC. These tradeoffs are further pronounced due to the non-linear load-stiffening and elastokinematic effects in distributed-compliance flexure mechanisms, which are nevertheless desirable due to elastic-averaging [11-12]. Load-stiffening refers to the increase in stiffness in the presence of loads, and elastokinematic effect characterizes the specific displacement component that has a kinematic dependence on other displacements as well as an elastic dependence on loads. While deterministic mathematical techniques for flexure design exist [13-14], these are best suited for shape and size synthesis. Constraint-based design has generally proven to be effective in flexure mechanism topology generation [15]. Accordingly, several new parallel kinematic XY flexure mechanisms based on a systematic and symmetric arrangement of common flexure modules, in a fashion that does not over-constrain the primary motions, have been proposed [11, 16]. Some representative designs, the underlying constraint pattern, key performance characteristics, and design challenges and tradeoffs are presented in this paper.

A closed-form non-linear analysis is employed to predict the performance of the proposed XY mechanisms, which utilize the standard double parallelogram flexure module. Although the presented analysis is valid for any general shape of the constituent beams in these modules, uniform-thickness simple beams are assumed for the purpose of illustration. Non-linearities associated with the beam curvature, which can be modeled using elliptical integrals [17] or the pseudo-rigid body method [18], have been neglected since deflections considered here are an order less the beam length. However, load-stiffening and elastokinematic non-linearities resulting from the deformed-state force equilibrium conditions can play a significant role in determining the influence of loads and displacements in one direction on the stiffness and error motion properties of other directions. Since these non-linearities can arise for displacements of

the order of the beam thickness and significantly influence the performance of a flexure mechanism, they cannot be ignored. Existing treatments of load-stiffening and elastokinematic effects in beams are either too complex for closed-form analysis [19] or case-specific [20]. Due to their assumed lumped-compliance topology, pseudo-rigid body models do not capture elastokinematic effects. Therefore, a generalized analytical formulation based on simple yet accurate approximations for the non-linear force-displacement relationships of the beam flexure [11-12] is used here.

A realistic performance prediction, not possible using a linear analysis, is thus obtained without the need for iterative or numerical methods. The parametric nature of these results offers several insights into XY flexure mechanism design, particularly in terms of performance characteristics and compromises therein. The presented analyses also provide a mathematical verification of the design axiom that geometric symmetry in mechanism design yields improved performance. To verify the analytical predictions, an experimental setup has been designed that accommodates multiple sensors and actuators to reliably characterize one of the proposed XY flexure mechanism designs.

2. XY Mechanism Topology Design

There are two kinds of design configurations for multi-DOF mechanisms – serial and parallel. Serial designs present a stacked assembly of several single-DOF stages and incorporate moving actuators and cables, which can be detrimental for precision and dynamic performance. Parallel designs, which are considered here, are usually compact and allow ground mounting of actuators. While the generic performance characteristics of flexures such as mobility, error motions and stiffness variations have been defined in the prior literature [12], the specific desirable attributes of a parallel kinematic XY flexure mechanism and associated challenges are listed here.

1. The primary objective of the design is to achieve large ranges of motion along the desired directions X and Y, and an obvious limitation comes from material failure criteria. For a given maximum stress level, high compliance in the directions of primary motion or DOF increases the range of motion. However, in designs with out-of-plane constraints, this conflicts with the need to maintain high stiffness and small error motions in the out-of-plane directions, thus making planer designs preferable.

2. In an XY mechanism, the motion stage yaw is often undesirable. Given this requirement, the motion stage yaw may be rejected passively or actively. While both options have respective advantages, fewer actuators make the former favorable due to reduced design complexity and potentially better motion range. Thus, the mechanism has to be designed such that the rotation of the motion stage, being a *parasitic error motion*, is inherently constrained. This error motion may be further attenuated by exploiting the *Center of Stiffness* (COS) concept to appropriately place the actuators, as explained in the following section.

3. Minimal *cross-axis coupling* between the X and Y degrees of freedom is an important performance requirement, especially in applications where end-point feedback is not feasible or the two axes are not actively controlled. Cross-axis coupling refers to any motion along the Y direction in response to an actuation along the X direction, and vice versa. In the absence of end-point feedback, it necessitates an additional calibration step to determine the transformation matrix between the actuator coordinates and the motion stage coordinates. In unactuated or under-actuated systems, cross-axis coupling can lead to undesirable internal resonances.

4. An important challenge in parallel mechanism design for positioning is that of integrating the ground-mounted actuators with the motion stage. Linear displacement or force source actuators typically do not tolerate transverse loads and displacements. Therefore, the point of actuation on the flexure mechanism must be such that it only moves along the direction of actuation and has minimal transverse motions in response to any actuator in the system. Eliminating transverse motion at the point of actuation, is termed as *actuator isolation*, and is generally difficult to achieve due to the parallel geometry.

5. In the absence of adequate actuator isolation, the actuators have to be connected to the point of actuation by means of a decoupler, which ideally transmits axial force without any loss in motion and absorbs any transverse motions without generating transverse loads. However, a flexure-based decoupler, which is desirable to maintain precision, is subject to its own tradeoffs. Increasing its motion range and compliance in the transverse direction results in *lost motion* between the actuator and motion stage, affecting precision, and loss in stiffness along its axial direction. The latter contributes to *drive stiffness*, which is the overall stiffness between the point of actuation and the motion stage, and influences the dynamic performance of the motion system.

6. Low thermal and manufacturing sensitivities are important performance parameters for precision flexure mechanisms in general. Both these factors, being strongly dependent on the mechanism's geometry, may be improved by careful use of reversal and symmetry.

Because of the tradeoff between quality of DOF and DOC, all these performance measures including parasitic errors, cross-axis coupling, actuator isolation, lost motion and drive stiffness, deteriorate with increasing range of motion, as shall be shown quantitatively in the subsequent sections. Depending upon the application, these collectively restrict the range of a parallel kinematic mechanism to a level much smaller than what is allowed by material limits. While geometric symmetry plays an important role in improving performance, it can overconstrain the primary directions resulting in a significantly reduced range, if implemented inappropriately.
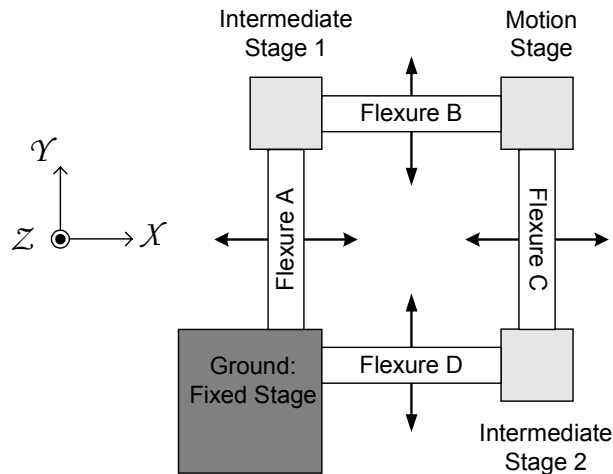

Fig.1 Proposed Constraint Arrangement for XY Flexure Mechanisms

Fig. 1 illustrates the proposed constraint arrangement that can help achieve the above-listed desirable attributes in XY mechanisms. The constraint arrangement includes four basic rigid stages: Ground, Motion Stage, and intermediate Stages 1 and 2. Stage 1 is connected to ground by means of flexure module A, which only allows relative X translation; the Motion Stage is connected to Stage 1 via flexure module B, which only allows relative Y translation; the Motion Stage is connected to Stage 2 via flexure module C, which only allows a relative X translation; and finally, Stage 2 is connected to Ground by means of flexure module D, which only allows relative Y translation. Thus, in any deformed configuration of the mechanism, Stage 1 will always have only an X displacement with respect to Ground while Stage 2 will have only a Y

displacement. Furthermore, the Motion Stage inherits the X displacement of Stage 1 and the Y displacement of Stage 2, thus acquiring two translational degrees of freedom that are mutually independent. Since the Y and X displacements of the Motion Stage do not influence Stage 1 and Stage 2, respectively, these are ideal locations for applying the actuation loads, obviating the need for decouplers.

In an ideal scenario where the flexure modules A, B, C and D are perfect constraints, this arrangement would yield a flawless design. However, due to the inherent imperfection in flexures, the actual resulting designs are expected to deviate slightly from ideal behavior. Any approximately linear motion flexure module can be used as the building-blocks A, B, C and D. Fig. 2 presents a design based on the double parallelogram flexure module. Although simple beams are illustrated, other beam shapes may be employed as well. The double parallelogram flexure offers large range, good rotational stiffness, no purely kinematic parasitic errors, and excellent thermal stability.
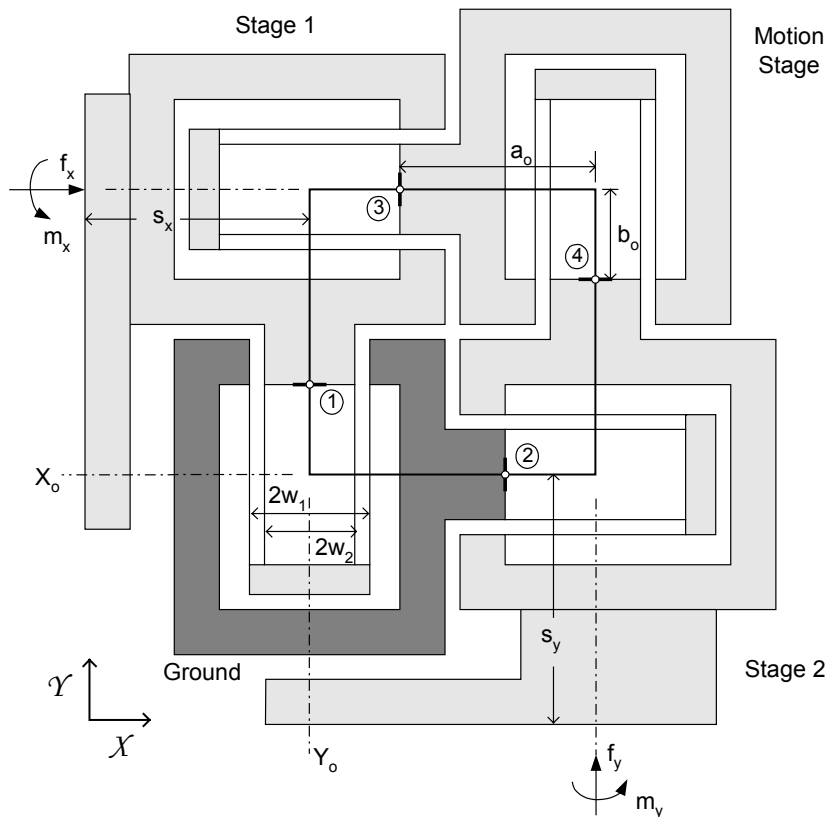

Fig.2 XY Flexure Mechanism Design 1

Without causing overconstraint, this design is further enhanced by making use of symmetry, which involves adding intermediate Stages 3 and 4, and repeating the constraint arrangement described earlier. The resulting design, illustrated in Fig. 3, is expected to exhibit superior performance. Since the relative rotation in the double parallelogram module is elastic and elastokinematic in nature, motion stage rotation in both these mechanisms may be mitigated by appropriately locating the actuation forces on the intermediate stages [12]. The axes of X and Y actuation that minimize the motion stage yaw are referred to as the *Center of Stiffness* axes.
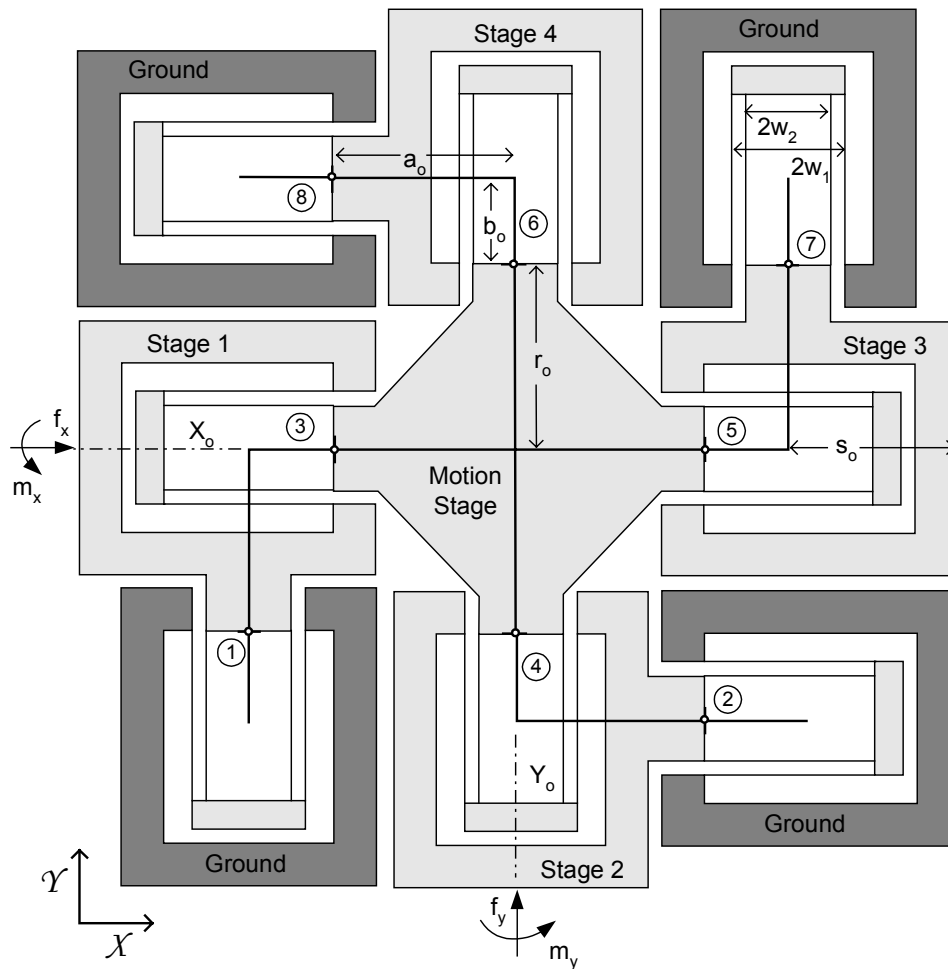

Fig.3 XY Flexure Mechanism Design 2

At this point, it is interesting to highlight the inadequacy of the traditional mobility criteria in determining the DOF of flexure mechanisms. Gruebler's criterion predicts a DOF of *1* for Design 1, and *–1* for Design 2. In other words, Design 1 should only allow a single independent

actuation, while Design 2 should be immobile due to over-constraint. Both these predictions are incorrect because the geometric constraint arrangement in each of these cases results in redundant constraints. In rigid-link mechanisms, geometric imperfections arising from manufacturing and assembly, can cause otherwise redundant constraints to become independent, a possibility that is accurately captured by Gruebler's criterion. However, in flexure mechanisms, particularly distributed-compliance topologies, elastic averaging plays an important role in ensuring that redundant constraints remain unaffected despite small geometric variations. Elastic averaging is a consequence of finite stiffness along the constraint directions in flexures. Thus, while the lack of ideal constraint behavior in flexures results in performance compromises on one hand, it is also responsible for allowing special geometries in mechanism topology design.

Several other XY designs with different space utilization, choice of building-blocks, and levels of symmetry can be generated using the proposed constraint arrangement [16]. The performance of any resulting mechanism depends on the constraint characteristics of the individual building-blocks and the geometry of the constraint arrangement, as shall be shown analytically in the following sections.

3. Performance Prediction of Proposed XY Mechanisms
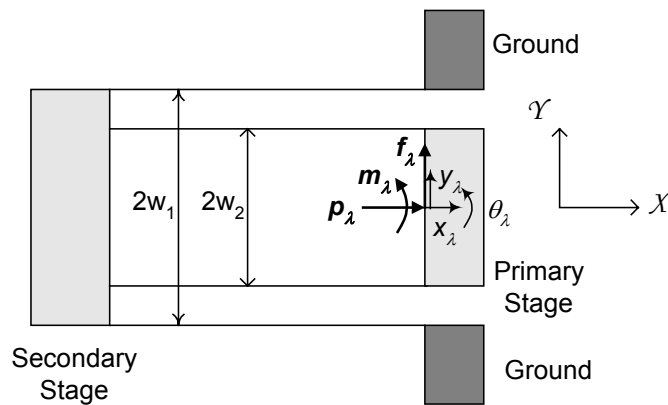

Fig.4 Double Parallelogram Flexure Module

It has been shown that the load-stiffening and elastokinematic non-linearities resulting from the deformed-state force equilibrium conditions significantly influence the constraint properties of beam-based flexure mechanisms. Accurate closed-form force-displacement relationships that

incorporate these non-linearities have been derived for the double parallelogram flexure [12], and shall be used in the analysis of the proposed XY mechanisms. With reference to Fig. 4, the linear and non-linear force-displacement results for the double parallelogram flexure are reproduced below.

Linear Analysis:

$$
\begin{bmatrix} y_\lambda \\ \theta_\lambda \\ x_\lambda \end{bmatrix} = \begin{bmatrix} \frac{1}{a} & \frac{1}{2\bar{w}^2 d} & 0 \\ \frac{1}{2\bar{w}^2 d} & \frac{1}{\bar{w}^2 d} & 0 \\ 0 & 0 & \frac{1}{d} \end{bmatrix} \begin{bmatrix} f_\lambda \\ m_\lambda \\ p_\lambda \end{bmatrix} \quad \text{where} \quad \bar{w}^2 \triangleq \frac{2w_1^2 w_2^2}{w_1^2 + w_2^2}
\tag{1}
$$

Non-Linear Analysis:

$$
y_\lambda \approx \frac{4af_\lambda}{(2a)^2 - (ep_\lambda)^2}
$$

$$
\theta_\lambda \approx \frac{1}{2w_1^2}\left(\frac{1}{d} + \frac{f_\lambda^2}{(2a - p_\lambda e)^2} r \right)\left[m_\lambda - \frac{f_\lambda}{(2a - p_\lambda e)}\left(1 - \frac{p_\lambda}{(2a + ep_\lambda)} + (2c - p_\lambda h) \right) \right]
$$

$$
+ \frac{1}{2w_2^2}\left(\frac{1}{d} + \frac{f_\lambda^2}{(2a + p_\lambda e)^2} r \right)\left[m_\lambda - \frac{f_\lambda}{(2a + p_\lambda e)}(2c + p_\lambda h) \right]
\tag{2}
$$

$$
x_\lambda = \frac{p_\lambda}{d} + p_\lambda y_\lambda^2 \frac{r\left[(2a)^2 + (ep_\lambda)^2 \right] - 8aei}{(4a)^2} \approx p_\lambda \left[\frac{1}{d} + \frac{y_\lambda^2}{2}\left(\frac{r}{2} - \frac{ei}{a} \right) \right]
$$

In the above expressions, f_λ, m_λ, p_λ, y_λ, θ_λ, and x_λ represent normalized transverse force, moment, axial force, transverse displacement, rotation, and axial displacement, respectively, for a given double parallelogram flexure module. All displacements and length parameters are normalized by the beam length L, forces by $E'I_{zz}/L^2$, and moments by $E'I_{zz}/L$. E' denotes Young's modulus for plane stress, and plate modulus for plane strain. The coefficients a, c, e, h, i and r are all non-dimensional numbers that are characteristic of the beam shape, and assume the following values for a simple beam with uniform thickness: $a=12$, $c=-6$, $e=1.2$, $h=-0.1$, $i=-0.6$, and $r=1/700$. Although simple beams are used for illustration, these force-displacement results and all the subsequent derivations are valid for any general beam shape.

The primary and secondary stages, along with ground, are assumed rigid in arriving at the above results. Therefore, the normalized elastic axial stiffness of the double parallelogram module is

simply given by the elastic axial stiffness of the constituent beams, d. For a simple beam, d assumes a value of $12/t^2$, where t is the normalized beam thickness. If the dimensions of the primary, secondary or ground stages are such that they cannot be assumed perfectly rigid, additional elastic stiffness or compliance contributions should be included in the above expressions. This primarily affects the axial stiffness of the double parallelogram module.

In analyzing the two proposed XY mechanism designs, force equilibrium is applied in the deformed configuration of the mechanism to capture the relevant non-linearities. Ground, Motion Stage and the Intermediate Stages are all assumed perfectly rigid. For typical dimensions, the transverse elastic stiffness, a, of the beam is several orders of magnitude smaller than its axial elastic stiffness, d, and may generally be neglected in comparison. Being small, rotations may also be neglected wherever their contribution is relatively insignificant. All non-dimensional quantities are represented by lower case alphabets throughout this paper.

3.1 XY Mechanism Design 1

XY Mechanism Design 1 is shown in a deformed configuration in Fig. 5, where the rigid frames including Ground, Motion Stage and the two intermediate stages are represented by solid lines, and the compliance of the double parallelograms is denoted by the small circles. The planer rotations of the Motion Stage and the two intermediate stages are exaggerated for the purpose of illustration. Free Body Diagrams of the individual stages are also included. The relative displacements of each constituent flexure module are given by,

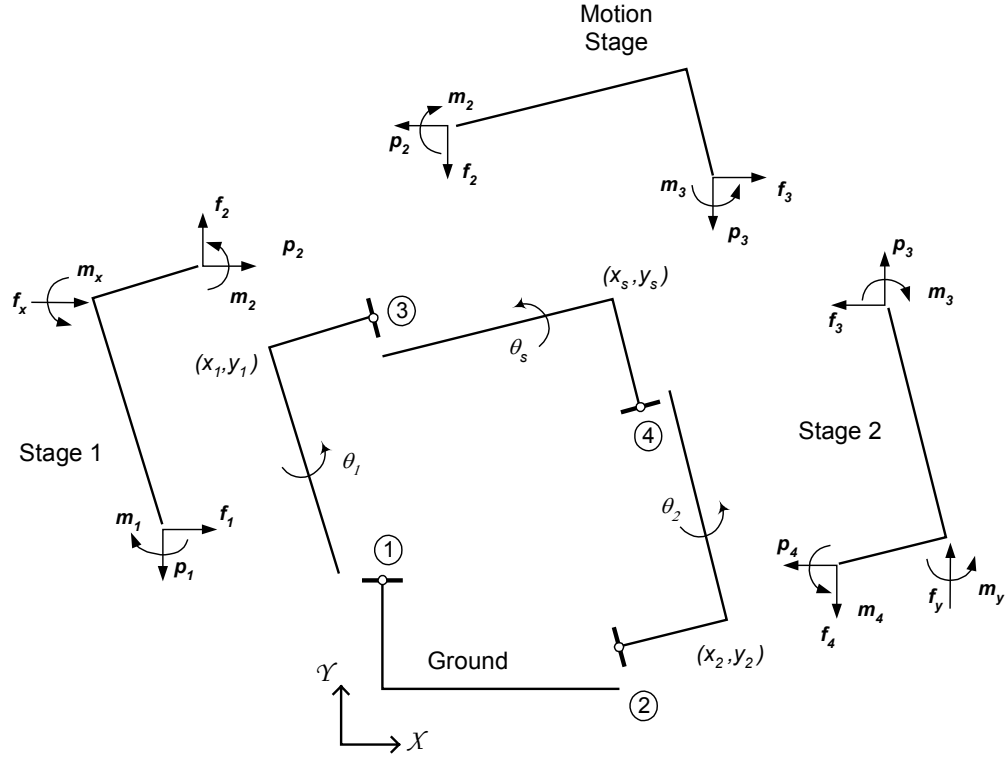| λ	θ_λ	y_λ	x_λ
1	θ_1	$x_1 + a_o\theta_1$	y_1
2	θ_2	$y_2 - b_o\theta_2$	x_2
3	$\theta_s - \theta_1$	$(y_s - a_o\theta_s) - (y_1 + b_o\theta_1)$	$x_s - x_1$
4	$\theta_s + \theta_2$	$(x_2 - a_o\theta_2) - (x_s + b_o\theta_s)$	$y_s - y_2$

Fig.5 XY Mechanism 1 in a Deformed Configuration

There are three internal forces per flexure module and three displacements per stage, resulting in 21 unknowns. The three force-displacement relations per flexure module, given by (1), and three force-equilibrium relations per stage provide 21 equations. Since the internal forces are not of interest, instead of solving these equations explicitly, energy methods are employed to efficiently obtain the following summarized force-displacement results for the linear case.

$$
\begin{Bmatrix} f_x \\ f_y \\ m_x \\ m_y \\ 0 \end{Bmatrix} = \begin{bmatrix} k_1 & 0 & -k_2 & -k_2 & -k_3 \\ 0 & k_1 & k_3 & k_3 & k_2 \\ -k_2 & k_3 & k_4 & 0 & -k_5 \\ -k_2 & k_3 & 0 & k_4 & -k_5 \\ -k_3 & k_2 & -k_5 & -k_5 & k_4 \end{bmatrix} \begin{Bmatrix} x_s \\ y_s \\ \theta_1 \\ \theta_2 \\ \theta_s \end{Bmatrix} \quad \text{where} \quad \begin{aligned} k_1 &= 2a \\ k_2 &= -a(a_o + \tfrac{1}{2}) \\ k_3 &= -a(b_o - \tfrac{1}{2}) \\ k_4 &= a(a_o^2 + b_o^2) - a(b_o - a_o) + 2\overline{w}^2 d \\ k_5 &= \tfrac{1}{2}a(b_o - a_o) - a(a_o b_o) \end{aligned} \tag{3}
$$

The Motion Stage rotation can be obtained by inverting the above stiffness matrix.

$$
\theta_s = \frac{1}{k_4}\big(m_x - f_x(a_o + b_o) + m_y + f_y(a_o + b_o)\big)
$$

This expression shows that the motion stage rotation can be made identically zero if $m_x = f_x(a_o + b_o)$ and $m_y = -f_y(a_o + b_o)$, which implies that the COS axes for the Motion Stage with

respect to the X and Y actuation forces is given by X_o and Y_o, shown in Fig. 2. Not being intuitively obvious, this is useful information if Motion Stage yaw is to be minimized passively. With this choice of actuation force locations, the remaining displacements can be calculated from the matrix expression (3).

$$x_s = \frac{f_x}{2a} + \frac{(2a_o+1)^2}{16\overline{w}^2 d}f_y \; ; \qquad x_1 = x_s + \frac{f_x}{2d} \; ; \qquad x_2 = \frac{f_x}{2d}$$

$$y_s = \frac{f_y}{2a} + \frac{(2b_o-1)^2}{16\overline{w}^2 d}f_x \; ; \qquad y_1 = \frac{f_y}{2d} \; ; \qquad y_2 = y_s + \frac{f_y}{2d}$$

$$\theta_1 = -\frac{(1-2a_o-4b_o)}{8\overline{w}^2 d}f_x - \frac{(1-2b_o)}{8\overline{w}^2 d}f_y$$

$$\theta_2 = -\frac{(1+2a_o)}{8\overline{w}^2 d}f_x - \frac{(1+4a_o+2b_o)}{8\overline{w}^2 d}f_y$$

(4)

Since the linear analysis captures only elastic effects, it should be recognized that these results are valid only for small loads and displacements. Nevertheless, they provide valuable design help not only in determining the actuator locations but also in selecting the geometric parameters a_o and b_o so as to minimize cross-axis coupling and intermediate stage rotations. In this case, the above results indicate that the dimension a_o should be kept as small as possible and b_o should be chosen to be *1/2*.

To accurately predict the elastokinematic effects that become prominent with increasing loads and displacements, we proceed to perform a non-linear analysis. The 21 equations, including the non-linear force displacement relations (2) for the double parallelogram, are explicitly solved using the symbolic computation tool MAPLE™. Taking advantage of the normalized framework, higher order small terms are dropped at appropriate steps in the analysis, and the following force-displacement results for the mechanism are obtained.

$$x_s = \frac{1}{(4a)^2 - (ef_y)^2}\left[8af_x + \frac{a^2(1+2a_o)}{\overline{w}^2 d}f_y - 8a^2\left(a_o\theta_1 + a_o\theta_2 + b_o\theta_s\right)\right]$$

(5)

$$y_s = \frac{1}{(4a)^2 - (ef_x)^2}\left[8af_y + \frac{a^2(1-2b_o)}{\overline{w}^2 d}f_x + 8a^2\left(b_o\theta_1 + b_o\theta_2 + a_o\theta_s\right)\right]$$

(6)

$$x_1 = x_s + \left[\frac{y_2^2(ra/2 - ei)}{4a} + \frac{1}{2d}\right]f_x \qquad ; \qquad y_1 = \left[\frac{x_1^2(ra/2 - ei)}{4a} + \frac{1}{2d}\right]f_y$$

(7)

$$y_2 = y_s + \left[\frac{x_1^2(ra/2 - ei)}{4a} + \frac{1}{2d} \right] f_y \qquad ; \qquad x_2 = \left[\frac{y_2^2(ra/2 - ei)}{4a} + \frac{1}{2d} \right] f_x \qquad (8)$$

While the results of the linear and non-linear analyses match exactly for small loads and displacements, it is apparent that the latter is necessary to predict several factors that contribute to the performance characteristics. Expressions (5) and (6) indicate that the primary motion stiffness drops as a quadratic function of the actuation force in the other direction. Over an approximate force range of ± 2.4 required to produce ± 0.1 displacements of the Motion Stage, the primary stiffness variation is less than 0.4%. This is illustrated in Fig. 6, which plots the closed-form analysis (CFA) results along with FEA results and confirms the large primary motion range and relatively invariant primary stiffness. Typical dimensions and material properties have been selected for the purpose of FEA, and are listed in Section 4.

The cross-axis coupling in both directions has linear as well as an inverse-quadratic components, and is influenced by the stage rotations. While the linear component in y_s in response to f_x may be eliminated by the choice of $b_o = 1/2$, no such remedy is available for the other direction. This is not surprising given the lack of symmetry between the X and Y axes in this design. Fig. 7 shows the extent of cross-axis coupling, which can be as large as 0.7% of the primary motion, over an actuation force range of ± 2.4.

Expressions (7) and (8) predict the degree of lost motion and drive stiffness. For a given Motion Stage X displacement, the intermediate Stage 1 experiences both an X displacement as well as a Y displacement in response to a Y actuation force. While the former is a consequence of the elastokinematic effects in double parallelogram 2 and contributes to lost motion, the latter results from the elastokinematic effect in double parallelogram 1 and hurts actuator isolation. The axial compliance of double parallelogram 2 contributes to the overall drive compliance between the X actuator and the motion stage, and is given by

$$\frac{\partial(x_1 - x_s)}{\partial f_x} = \frac{1}{2d} + \frac{y_2^2}{4}\left(\frac{r}{2} - \frac{ei}{a} \right) \qquad (9)$$

Lost motion and loss of drive stiffness, predicted above, are plotted in Fig. 8. Lost motion is less than 0.5% of the primary motion over the range of interest. Although not significant for small displacements, the predicted drop in axial stiffness is more than 90% from the nominal value for displacements of the order of ± 0.1 and is of concern for both static and dynamic performance.

To restrict the loss in drive stiffness to less than *25%*, the motion range of this design has to be limited to *± 0.0125*.

Actuator isolation is determined by the amount of Y displacement at the point of X force application. If the X force is applied along the COS axis, X_o, the extent of actuator isolation is given by $(y_l - s_x\theta_l)$, which is plotted in Fig. 9. The lack of actuator isolation for the Y actuator can be as large as *1.5%* of the primary motion for the force ranges of interest.
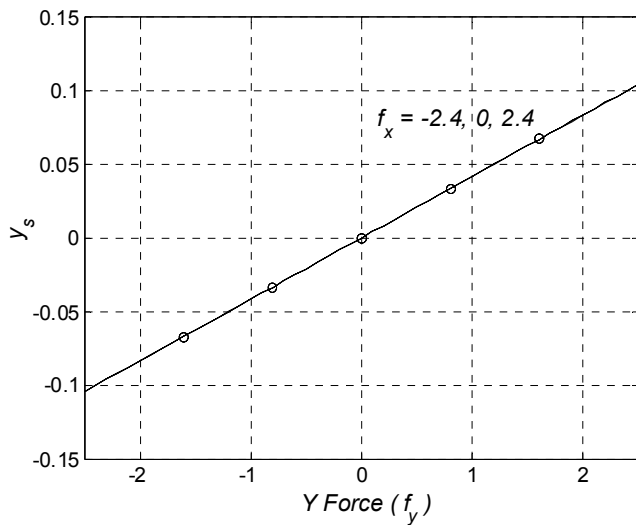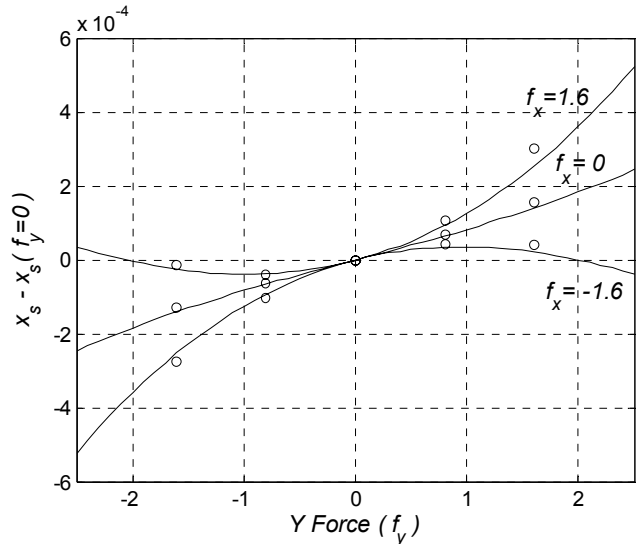

Fig.6 Primary Motion: : CFA (–) and FEA (o)

Fig.7 Cross-Axis Error Motion: CFA (–) and FEA (o)
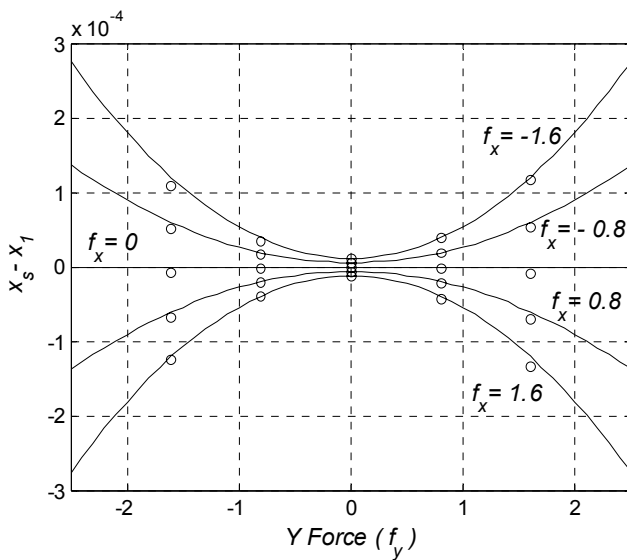

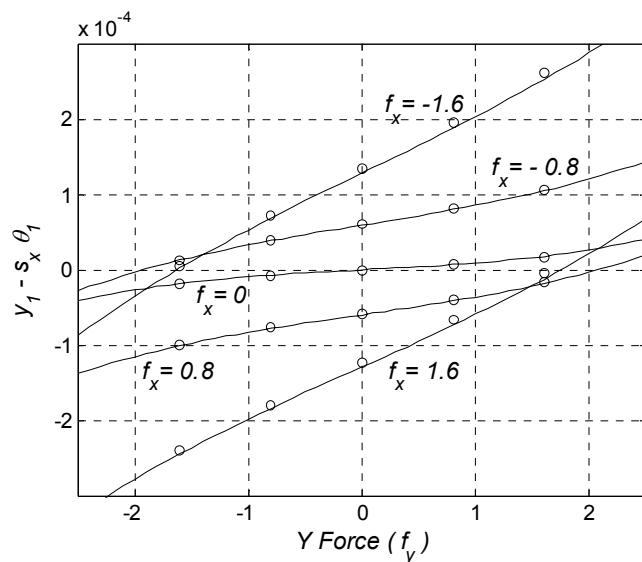*Fig.8 Lost Motion / Drive Stiffness: CFA (–) and FEA* (o)

Fig.9 Actuator Isolation: CFA (–) and FEA (o)

For simplicity, Motion Stage rotation is expressed here for two special cases.

$$\theta_s = \frac{1}{64a^2\overline{w}^2 d}\left[32a^2\left(\boldsymbol{m}_x - a_o\boldsymbol{f}_x - b_o\boldsymbol{f}_x\right) + rd\left(2\boldsymbol{m}_x - a_o\boldsymbol{f}_x - b_o\boldsymbol{f}_x\right)\boldsymbol{f}_x^2\right] \quad \text{for} \quad \boldsymbol{f}_y = 0 = \boldsymbol{m}_y$$

$$\theta_s = \frac{1}{64a^2\overline{w}^2 d}\left[32a^2\left(\boldsymbol{m}_y + a_o\boldsymbol{f}_y + b_o\boldsymbol{f}_y\right) + rd\left(2\boldsymbol{m}_y + a_o\boldsymbol{f}_y + b_o\boldsymbol{f}_y\right)\boldsymbol{f}_y^2\right] \quad \text{for} \quad \boldsymbol{f}_x = 0 = \boldsymbol{m}_x$$

(10)

For small loads and displacements, these expressions yield COS axes identical to those predicted by the linear analysis. With no independent moments, and actuation forces acting along axes X_o and Y_o, the Motion Stage rotation reduces to

$$\theta_s = \frac{r}{\overline{w}^2}\cdot\frac{\left(a_o + b_o\right)}{64a^2 + 2rd\left(\boldsymbol{f}_x^2 + \boldsymbol{f}_y^2\right)}\cdot\left[\boldsymbol{f}_x^3 + \boldsymbol{f}_x^2\boldsymbol{f}_y - \boldsymbol{f}_x\boldsymbol{f}_y^2 - \boldsymbol{f}_y^3\right]$$

$$+ \frac{1}{a^2 d}\cdot\left\{\frac{4}{\overline{w}^2}\left(ah - ce\right) - \frac{2}{w_2^2}\right\}\cdot\frac{\boldsymbol{f}_x\boldsymbol{f}_y}{32a^2 + rd\left(\boldsymbol{f}_x^2 + \boldsymbol{f}_y^2\right)}$$

(11)

This shows that while it is possible to entirely eliminate the linear, or purely elastic, component of the Motion Stage rotation by selecting the force locations, the same is not true for the non-linear elastokinematic components because the COS shifts with increasing loads. Since the applied moments cannot be controlled independent of the forces, the mechanism's geometry plays an important role in the effectiveness of this passive yaw minimization method. Motion Stage rotation is plotted against the X and Y actuation forces in Fig. 10, which not only illustrate the inadequacy of the linear analysis but also provide an idea of the range beyond which the non-linear effects become important. For the chosen mechanism dimensions, the maximum rotation is approximately *40* μrad over a motion range of ± *0.1*. To ensure a motion stage rotation of less than *5* μrad, the motion range of this design is restricted to ± *0.05*.

Sensitivity of the Motion Stage yaw to the location of force application may also be analytically determined to simulate assembly and manufacturing tolerances that can cause an offset between the COS axis and the actual actuation axis. If e_x represents this offset, then the Motion Stage yaw is given by the following expression in the absence of any Y actuation.

$$\theta_s = \frac{1}{64a^2\overline{w}^2}\left[r\left(a_o + b_o + 2e_x\right)\boldsymbol{f}_x^3 + \frac{32a^2 e_x}{d}\boldsymbol{f}_x\right]$$
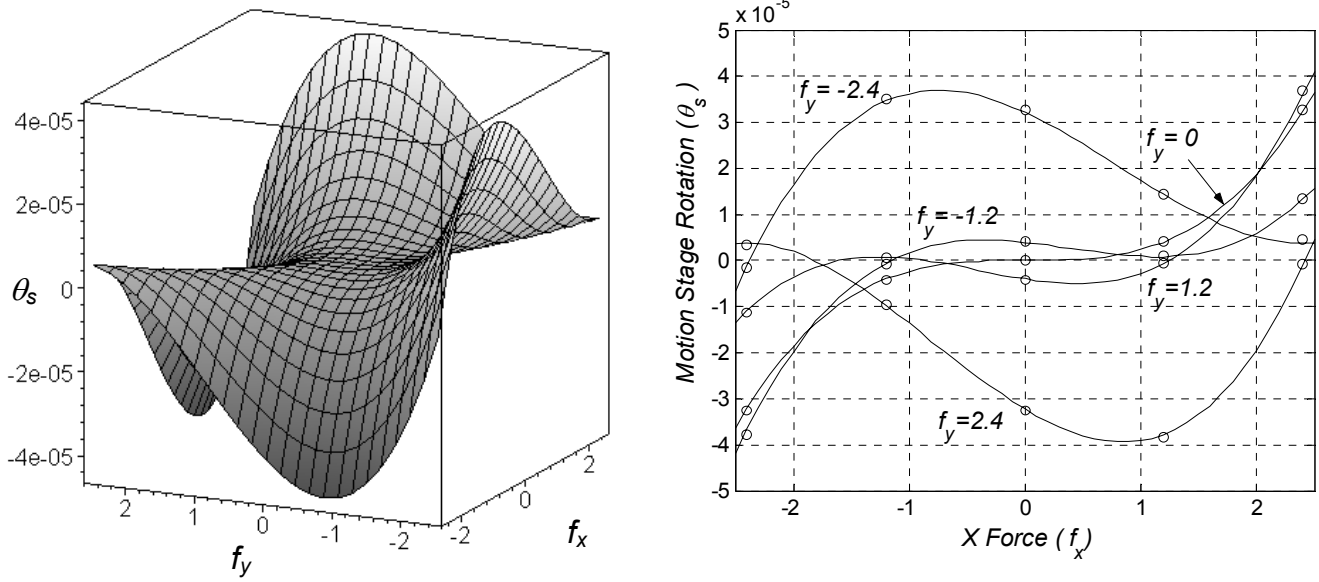
(12)

Fig.10 Motion Stage Rotation: CFA (Contour), CFA (–) and FEA (o)

Result (12) is corroborated by FEA in Fig. 11, where f_x is kept fixed at *0.25*. This picture will obviously change with increasing loads and in the presence of f_y.
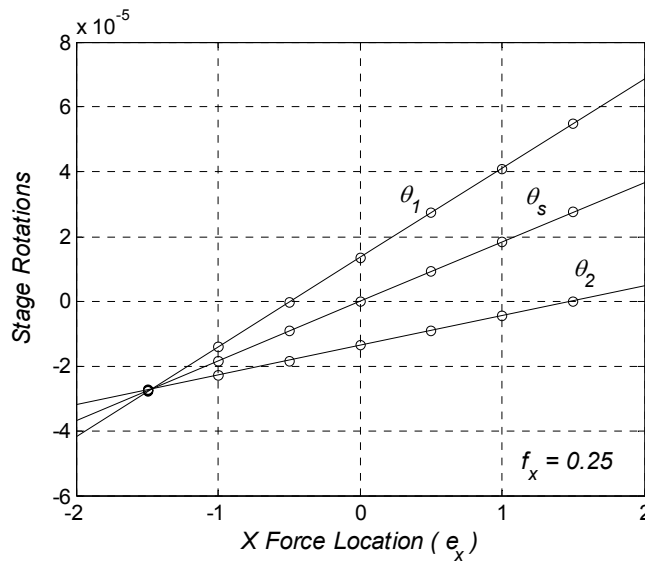

Fig.11 Moment Sensitivity and COS for the Stages with respect X Force: CFA (–) and FEA (o)

With the actuation forces applied along the COS of the Motion Stage, the intermediate stage rotations are calculated using the non-linear analysis for specific cases.

$$\theta_1 = \frac{1}{64a^2 \overline{w}^2 d} \left(\frac{rdf_x^2 + 16a^2}{rdf_x^2 + 32a^2} \right) \left[-16a^2 \left(1 - 2a_o - 4b_o\right) f_x + rd\left(a_o + b_o\right) f_x^3 \right] \qquad \text{for } f_y = 0$$

$$\theta_1 = \frac{1}{4\overline{w}^2 d \left(rdf_y^2 + 32a^2\right)} \left[16a^2 \left(2b_o - 1\right) f_y - rd\left(a_o - b_o + 1\right) f_y^3 \right] \qquad \text{for } f_x = 0$$

(13)

$$\theta_2 = \frac{1}{4\overline{w}^2 d \left(rdf_x^2 + 32a^2\right)} \left[-16a^2 \left(1 + 2a_o\right) f_x - rd\left(a_o - b_o + 1\right) f_x^3 \right] \qquad \text{for } f_y = 0$$

$$\theta_2 = \frac{1}{64a^2 \overline{w}^2 d} \left(\frac{rdf_y^2 + 16a^2}{rdf_y^2 + 32a^2} \right) \left[-16a^2 \left(1 + 2b_o + 4a_o\right) f_y - rd\left(a_o + b_o\right) f_y^3 \right] \qquad \text{for } f_x = 0$$

(14)

The intermediate stage rotations are obviously large and have a dominant linear component, with the non-linear contribution two orders of magnitude smaller. The dependence of Stage 1 rotation on f_y is clearly attenuated with the choice of $b_o = 1/2$. This is not true of Stage 2, which therefore sees a higher maximum rotation. The difference between the rotations of the two intermediate stages is due to the lack of symmetry in this design. These rotations are plotted in Figures 12 and 13 for various loading conditions.

If the application so demands, the actuation forces may be alternatively applied along the COS axes of Stage 1 or Stage 2, but this obviously affects the Motion Stage rotation. Both the linear as well as non-linear analyses reveal that the COS for Stage 1 with respect to X actuation force is located at a distance $(1 + 2b_o + 4a_o)/6$ from the nominal location, and with respect to the Y actuation force is located at $(1 - 2a_o - 4b_o)/2$, which actually corresponds to the Y_o axis for $b_o = 0.5$. Similarly, the COS of Stage 2 with respect to the Y actuation force is located at a distance $(1 - 2a_o - 4b_o)/6$ from the nominal location, and with respect to X actuation force is located at $(1 + 2b_o + 4a_o)/2$. A force location that results in a positive moment, following the convention of Fig. 2, is considered positive and vice versa. These results are also precisely validated by FEA in Fig. 11.

Thus, it is seen that XY Mechanism Design 1 offers a good range of primary motions, although other performance attributes such as cross-axis coupling, parasitic rotations, actuator isolation and drive stiffness deteriorate with increasing primary motion. Improvements in performance may be achieved by applying the actuation forces along the COS axes and choosing geometric parameters judiciously. Given its compact geometry, this design may be quite suitable for several applications.
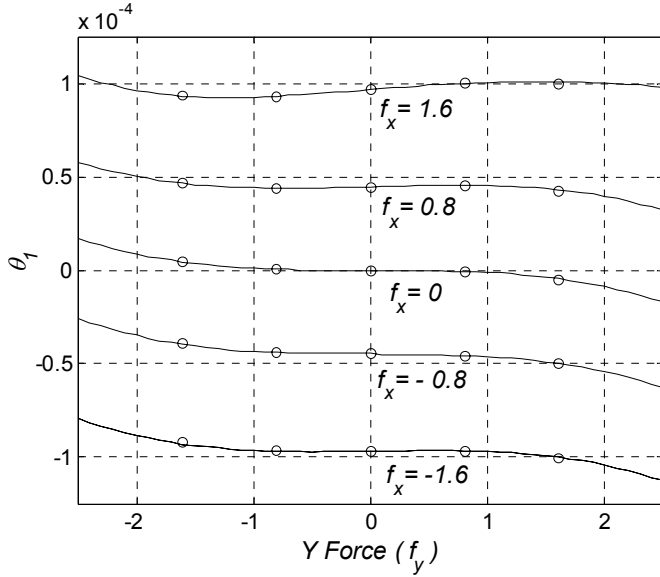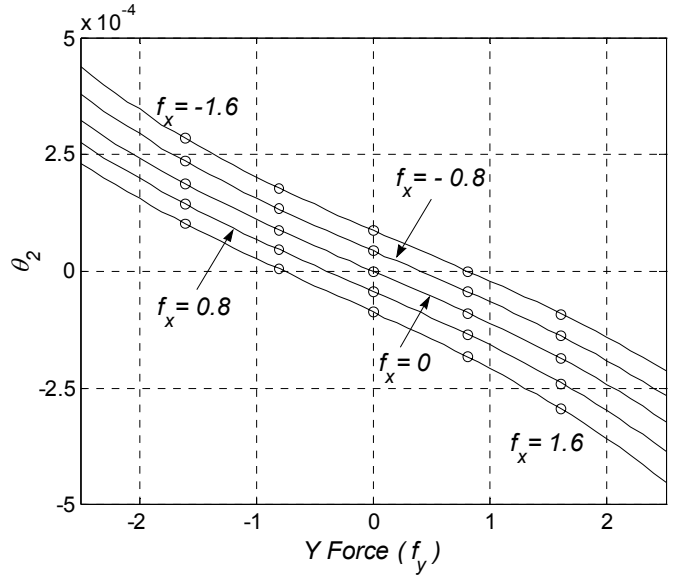
Fig.12 Stage 1 Rotation: CFA (–) and FEA (o)

Fig.13 Stage 2 Rotation: CFA (–) and FEA (o)

3.2 XY Mechanism Design 2

Fig. 14 illustrates the XY Mechanism Design 2 in a deformed configuration, along with the FBD and displacements of the stages. As in the previous case, stage rotations are exaggerated. The relative displacements for the individual double parallelogram flexure modules, represented by the small circles, are given by

λ	θ_λ	y_λ	x_λ
1	θ_1	$x_1 - a_o\theta_1$	y_1
2	θ_2	$y_2 + a_o\theta_2$	$-x_2$
3	$\theta_s + \theta_1$	$(y_s - r_o\theta_s) - (y_1 - b_o\theta_1)$	$x_s - x_1$
4	$\theta_s + \theta_2$	$-(x_s + r_o\theta_s) + (x_2 + b_o\theta_2)$	$y_s - y_2$
5	$\theta_s - \theta_7$	$-(y_s + r_o\theta_s) + (y_7 - b_o\theta_7)$	$-x_s + x_7$
6	$\theta_s - \theta_8$	$(x_s - r_o\theta_s) - (x_8 + b_o\theta_8)$	$-y_s + y_8$
7	θ_7	$x_7 - a_o\theta_7$	$-y_7$
8	θ_8	$y_8 - a_o\theta_8$	x_8

There are 3 unknown displacements per stage and 3 unknown internal forces per flexure module, resulting in 39 unknowns. The 3 force equilibrium relations per stage and 3 constitutive relations per flexure module provide 39 equations necessary to solve these unknowns.
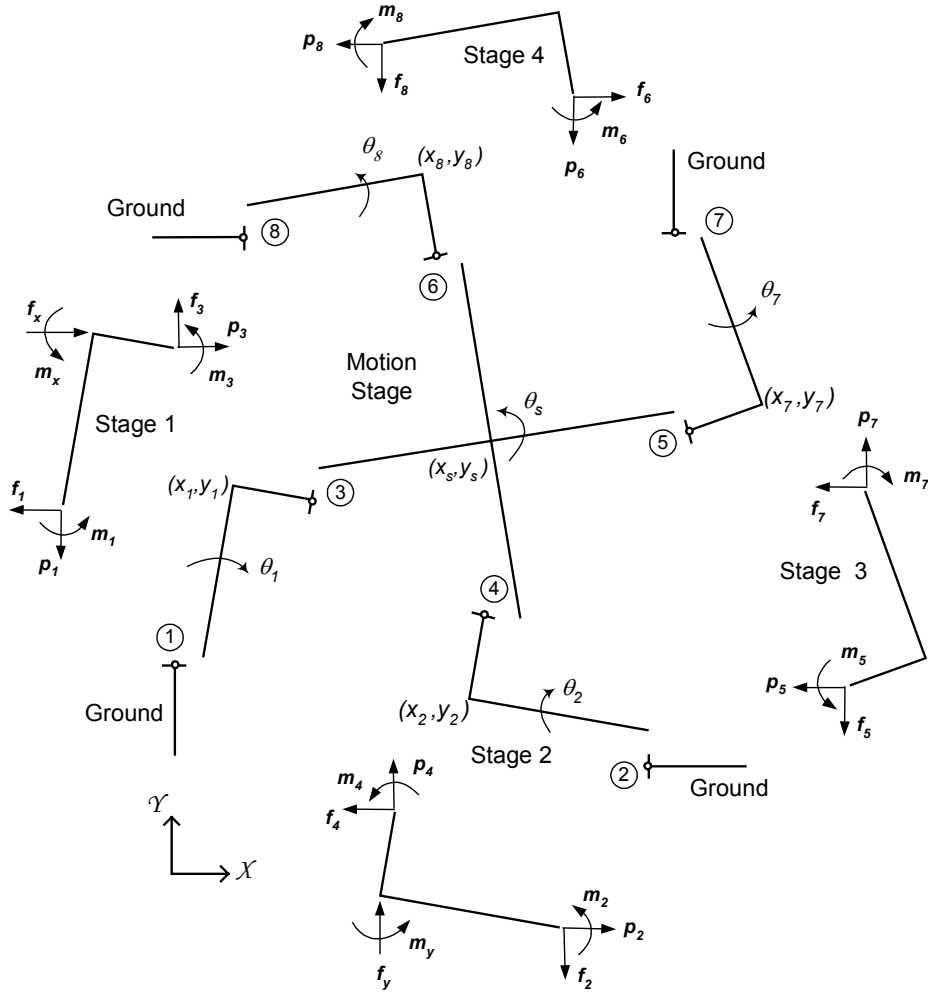
Fig.14 XY Mechanism 2 in a Deformed Configuration

As earlier, a linear analysis is performed first, using the linear constitutive relations (1) for the modules, which yields the following force-displacement results for the overall mechanism.

$$
\begin{bmatrix}
k_1 & 0 & k_2 & k_3 & k_2 & k_3 & 0 \\
0 & k_1 & -k_3 & k_2 & -k_3 & k_2 & 0 \\
k_2 & -k_3 & k_4 & 0 & 0 & 0 & -k_5 \\
k_3 & k_2 & 0 & k_4 & 0 & 0 & -k_5 \\
k_2 & -k_3 & 0 & 0 & k_4 & 0 & k_5 \\
k_3 & k_2 & 0 & 0 & 0 & k_4 & k_5 \\
0 & 0 & -k_5 & -k_5 & k_5 & k_5 & k_6
\end{bmatrix}
\begin{Bmatrix}
x_s \\ y_s \\ \theta_1 \\ \theta_2 \\ \theta_7 \\ \theta_8 \\ \theta_s
\end{Bmatrix}
=
\begin{Bmatrix}
\boldsymbol{f}_x \\ \boldsymbol{f}_y \\ -\boldsymbol{m}_x \\ -\boldsymbol{m}_y \\ 0 \\ 0 \\ 0
\end{Bmatrix}
\quad \text{where,} \quad
\begin{aligned}
k_1 &= 4a \\
k_2 &= -a(a_o + \tfrac{1}{2}) \\
k_3 &= -a(b_o - \tfrac{1}{2}) \\
k_4 &= a(a_o^2 + b_o^2) - a(b_o - a_o) + 2\overline{w}^2 d \\
k_5 &= ab_o(r_o + \tfrac{1}{2}) + (\tfrac{1}{2}ar_o + \overline{w}^2 d) \\
k_6 &= 4ar_o(r_o + \tfrac{1}{2}) + 4(\tfrac{1}{2}ar_o + \overline{w}^2 d)
\end{aligned}
$$

These equations may be further solved to determine the displacements explicitly.

$$x_s = \frac{f_x}{4a} - \frac{(2a_o + 1)m_x}{16d\overline{w}^2} - \frac{(2b_o - 1)m_y}{16d\overline{w}^2}; \quad x_1 = x_s + \frac{3f_x}{4d}; \quad x_7 = x_s - \frac{f_x}{4d}$$

$$y_s = \frac{f_y}{4a} + \frac{(2b_o - 1)m_x}{16d\overline{w}^2} - \frac{(2a_o + 1)m_y}{16d\overline{w}^2}; \quad y_2 = y_s + \frac{3f_y}{4d}; \quad y_8 = y_s - \frac{f_y}{4d}$$

$$x_2 = \frac{f_x}{4d}; \quad x_8 = \frac{f_x}{4d}; \quad y_1 = \frac{f_y}{4d}; \quad y_7 = \frac{f_y}{4d} \tag{15}$$

$$\theta_1 = \frac{(2a_o + 1)f_x}{16d\overline{w}^2} - \frac{(2b_o - 1)f_y}{16d\overline{w}^2} - \frac{5m_x}{8d\overline{w}^2} - \frac{m_y}{8d\overline{w}^2}; \quad \theta_7 = \frac{(2a_o + 1)f_x}{16d\overline{w}^2} - \frac{(2b_o - 1)f_y}{16d\overline{w}^2} + \frac{m_x}{8d\overline{w}^2} + \frac{m_y}{8d\overline{w}^2}$$

$$\theta_2 = \frac{(2a_o + 1)f_y}{16d\overline{w}^2} + \frac{(2b_o - 1)f_x}{16d\overline{w}^2} - \frac{m_x}{8d\overline{w}^2} - \frac{5m_y}{8d\overline{w}^2}; \quad \theta_8 = \frac{(2a_o + 1)f_y}{16d\overline{w}^2} + \frac{(2b_o - 1)f_x}{16d\overline{w}^2} + \frac{m_x}{8d\overline{w}^2} + \frac{m_y}{8d\overline{w}^2}$$

$$\theta_s = \frac{m_x}{4d\overline{w}^2} + \frac{m_y}{4d\overline{w}^2}$$

Once again, several interesting observations can be made from this preliminary analysis. Motion Stage rotation is predicted to be identically zero in the absence of any applied moments, irrespective of the geometric dimensions. This implies that the COS axes of the motion stage correspond to X_o and Y_o, which coincide with the nominal actuation locations, as shown in Fig. 3. Furthermore, the elastic contribution in the error motions can be minimized by choosing the smallest possible a_o, and $b_o=1/2$. With this choice of design parameters, the above results also show that the rotations of intermediate stages 1 and 3 are not affected by the Y actuation force, and those of intermediate stages 2 and 4 are not affected by X actuation force. Also, these results claim that there should be a perfect decoupling between the two axes.

A more accurate prediction of the mechanism behavior is obtained by solving the system equations using the nonlinear force-displacement relations (2) for the modules. By neglecting insignificant terms at each step in the derivation, the following displacement results are obtained using MAPLE™.

$$x_s = \frac{f_x \left(64a^2 + y_2^2 e^3 i f_y^2\right)}{4a \left(64a^2 - 3e^2 f_y^2\right)} \approx \frac{f_x}{4a} \frac{64a^2}{\left(64a^2 - 3e^2 f_y^2\right)} \tag{16}$$

$$x_1 = \frac{f_x}{4a}\frac{64a^2}{\left(64a^2 - 3e^2 f_y^2\right)} + \frac{f_x}{4}\left\{\frac{y_2^2}{2}\left(\frac{r}{2} - \frac{ei}{a}\right) + \frac{1}{d}\right\}\frac{\left(192a^2 - 11e^2 f_y^2\right)}{\left(64a^2 - 3e^2 f_y^2\right)}$$

$$\approx \frac{f_x}{4a}\frac{64a^2}{\left(64a^2 - 3e^2 f_y^2\right)} + \frac{3f_x}{4}\left(-\frac{y_2^2 ei}{2a} + \frac{1}{d}\right) \tag{17}$$

$$x_7 = \frac{f_x}{4a}\frac{64a^2}{\left(64a^2 - 3e^2 f_y^2\right)} - \frac{f_x}{4}\left\{\frac{y_2^2}{2}\left(\frac{r}{2} - \frac{ei}{a}\right) + \frac{1}{d}\right\}\frac{\left(64a^2 - e^2 f_y^2\right)}{\left(64a^2 - 3e^2 f_y^2\right)}$$

$$\approx \frac{f_x}{4a}\frac{64a^2}{\left(64a^2 - 3e^2 f_y^2\right)} - \frac{f_x}{4}\left(-\frac{y_2^2 ei}{2a} + \frac{1}{d}\right) \tag{18}$$

$$x_2 = \frac{f_x}{4}\left\{\frac{y_2^2}{2}\left(\frac{r}{2} - \frac{ei}{a}\right) + \frac{1}{d}\right\} \tag{19} \qquad\qquad x_8 = \frac{f_x}{4}\left\{\frac{y_2^2}{2}\left(\frac{r}{2} - \frac{ei}{a}\right) + \frac{1}{d}\right\} \tag{20}$$

$$y_s = \frac{f_y}{4a}\frac{\left(64a^2 + x_1^2 e^3 i f_x^2\right)}{\left(64a^2 - 3e^2 f_x^2\right)} \approx \frac{f_y}{4a}\frac{64a^2}{\left(64a^2 - 3e^2 f_x^2\right)} \tag{21}$$

$$y_2 = \frac{f_y}{4a}\frac{64a^2}{\left(64a^2 - 3e^2 f_x^2\right)} + \frac{f_y}{4}\left\{\frac{x_1^2}{2}\left(\frac{r}{2} - \frac{ei}{a}\right) + \frac{1}{d}\right\}\frac{\left(192a^2 - 11e^2 f_x^2\right)}{\left(64a^2 - 3e^2 f_x^2\right)}$$

$$\approx \frac{f_y}{4a}\frac{64a^2}{\left(64a^2 - 3e^2 f_x^2\right)} + \frac{3f_y}{4}\left(-\frac{x_1^2 ei}{2a} + \frac{1}{d}\right) \tag{22}$$

$$y_8 = \frac{f_y}{4a}\frac{64a^2}{\left(64a^2 - 3e^2 f_x^2\right)} - \frac{f_y}{4}\left\{\frac{x_1^2}{2}\left(\frac{r}{2} - \frac{ei}{a}\right) + \frac{1}{d}\right\}\frac{\left(64a^2 - e^2 f_x^2\right)}{\left(64a^2 - 3e^2 f_x^2\right)}$$

$$\approx \frac{f_y}{4a}\frac{64a^2}{\left(64a^2 - 3e^2 f_x^2\right)} - \frac{f_y}{4}\left(-\frac{x_1^2 ei}{2a} + \frac{1}{d}\right) \tag{23}$$

$$y_1 = \frac{f_y}{4}\left\{\frac{x_1^2}{2}\left(\frac{r}{2} - \frac{ei}{a}\right) + \frac{1}{d}\right\} \tag{24} \qquad\qquad y_7 = \frac{f_y}{4}\left\{\frac{x_1^2}{2}\left(\frac{r}{2} - \frac{ei}{a}\right) + \frac{1}{d}\right\} \tag{25}$$

As in the previous case, the non-linear analysis predicts several important factors that determine the mechanism's performance characteristics that are not captured by the linear analysis. Due to twice the number of double parallelogram modules, the normalized force required to generate a nominal primary motion of $\pm$ *0.1* in this case is approximately *4.8*, twice that for Design 1. Fig. 15 confirms the large primary motion, which follows a predominantly linear behavior and is free

of any over-constraining effects. It may be noticed in expression (16) that the primary stiffness in the X direction changes with the Y force. This is expected because upon the application of a positive Y force, flexure modules 4, 6 and 7 experience a compressive axial force, while module 1 sees a tensile axial force. Irrespective of whether the axial force is tensile or compressive, the transverse stiffness of all these modules drops resulting in an overall reduction in the primary motion stiffness. However, over the range of the applied forces, the drop in primary motion stiffness is less than *1.2%*, which is barely noticeable in FEA results and experimental measurements plotted in Fig. 15. The geometric dimensions and material properties of the mechanism used in the FEA and experimental testing are listed in the following section.

Expressions (16) and (21) show that the linear elastic component of the cross-axis coupling in this case is entirely eliminated. Any contributions from the applied moments and stage rotations are also cancelled out due to symmetry. However, there remains a quadratic elastokinematic component comparable to that in Design 1, and is plotted in Fig. 16. The worst-case cross-axis error is on the order of *1%* of the primary motion. Lost motion and change in drive stiffness are given by expressions (17) and (21). Being approximately two orders smaller than the next larger terms, the higher order terms in these expressions may be neglected. As in Design 1, the drive stiffness between the actuator and Motion Stage reduces with increasing primary motions owing to the double parallelogram characteristics. These predictions are validated in Fig. 17 by means of FEA and experimental measurements. Maximum lost motion is approximately *1%* of the primary motion, while the drop in drive stiffness is the same as in the previous case. Clearly, these attributes are not significantly affected by the overall mechanism's geometric layout, and are strongly dependent on the characteristics of the constraint building-blocks.

The degree of actuator isolation is given by the amount of X displacement at the point of Y actuation on Stage 2. This is given by *($x_2 - s_o \theta_2$)* and is comprised of linear and quadratic components. The quadratic component results from the elastokinematic effect in double parallelogram flexure module 2, derived in expression (19), in response to an X actuation force and Y primary motion. Actuator isolation is plotted in Fig. 18 and is shown to be up to *0.6%* of primary motion, which is similar to the previous design.
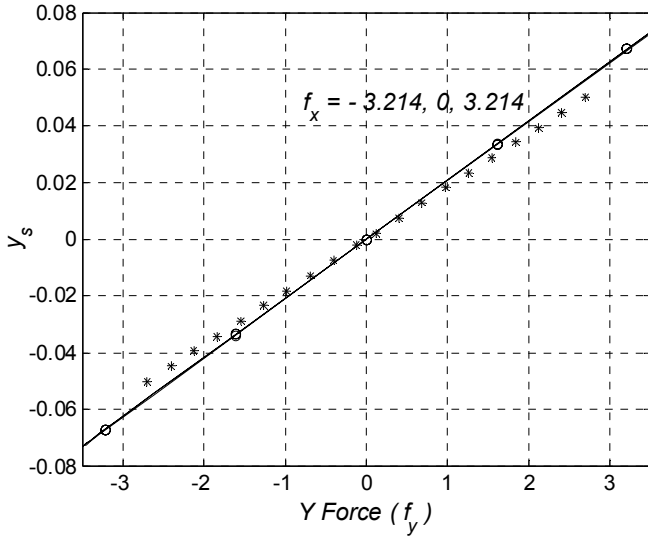
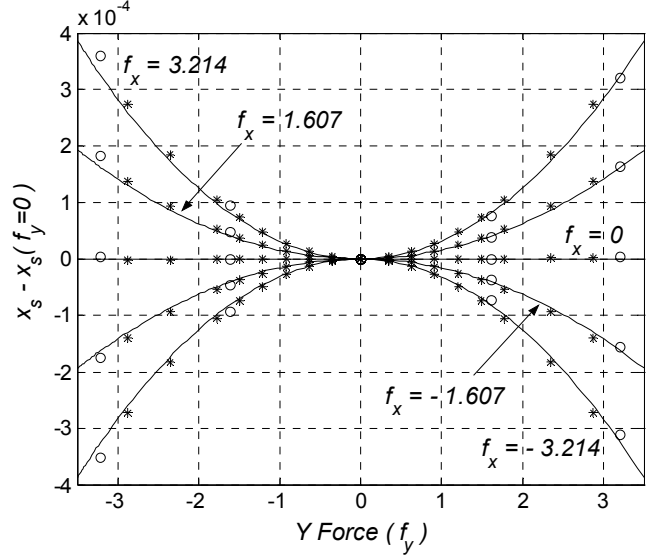Fig.15 Primary Motion: CFA (–), FEA (o), Exp (*)

Fig.16 Cross-axis Error Motion: CFA (–), FEA (o), Exp (*)
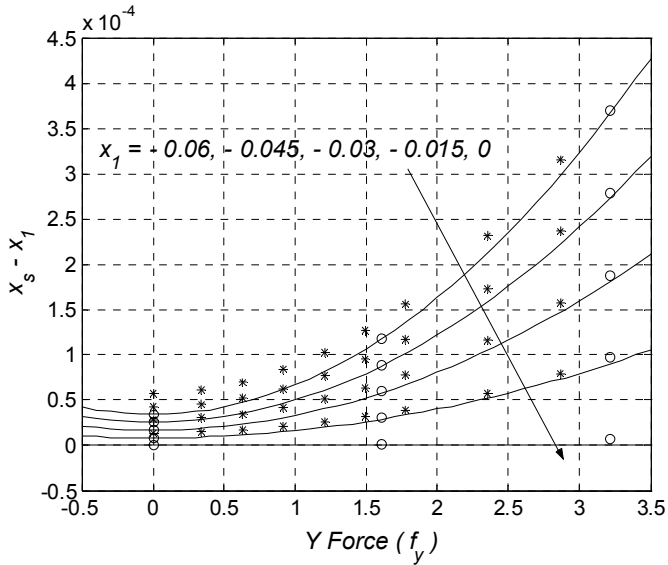

Fig.17 Lost Motion / Drive Stiffness: CFA (–), FEA (o), Exp (*)
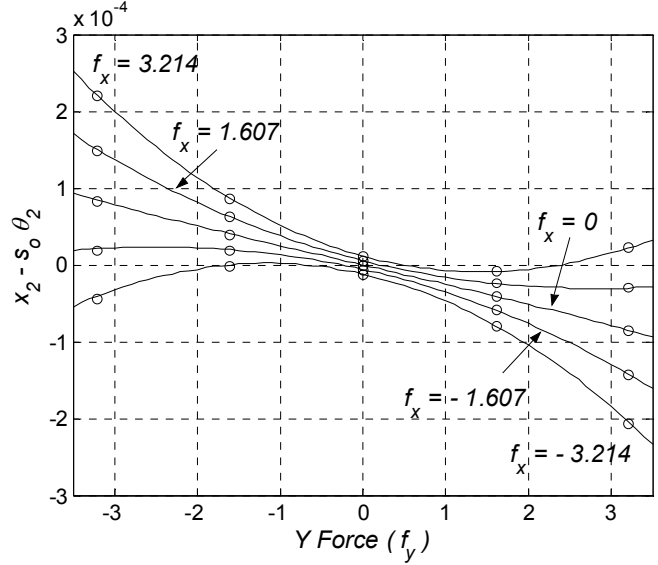
Fig.18 Actuator Isolation: CFA (–), FEA (o), Exp (*)

Next, the stage rotations can also be analytically calculated and the non-linear results are presented here for some specific cases. Motion Stage rotation is given by

$$\theta_s = \frac{\left(64a^2 + rd\boldsymbol{f}_x^2\right)}{256a^2\overline{w}^2d}\boldsymbol{m}_x \quad \text{for } \boldsymbol{f}_y = 0 = \boldsymbol{m}_y \quad \text{and} \quad \theta_s = \frac{\left(64a^2 + rd\boldsymbol{f}_y^2\right)}{256a^2\overline{w}^2d}\boldsymbol{m}_y \quad \text{for } \boldsymbol{f}_x = 0 = \boldsymbol{m}_x \quad (26)$$

This validates the inference drawn from the linear analysis regarding the COS location. Remarkably, this choice of COS axes which corresponds to $m_x = m_y = 0$ not only eliminates the linear elastic component in the Motion Stage rotation, but also some of the non-linear terms. The overall dependence of Motion Stage rotation on the X and Y actuation forces is presented in Fig. 19. From the large flat area in the central region of the 3D contour, it is apparent that the Motion Stage rotation has been considerably suppressed despite the elastokinematic errors of the double parallelogram flexure module. In fact, it is possible to keep the motion stage rotation less than *5* μrad over the entire motion range of ± *0.1* in both directions. Given the considerably small magnitude of the Motion Stage rotation, the accuracy of both the closed-form as well as finite element analyses is expected to be limited. Nevertheless, Fig. 19 indicates a fair agreement between the two analysis methods, in terms of magnitudes and trends. Experimental measurements of the stage rotation yielded a random variation within ± *10* μrad, which is very likely due to extraneous factors.
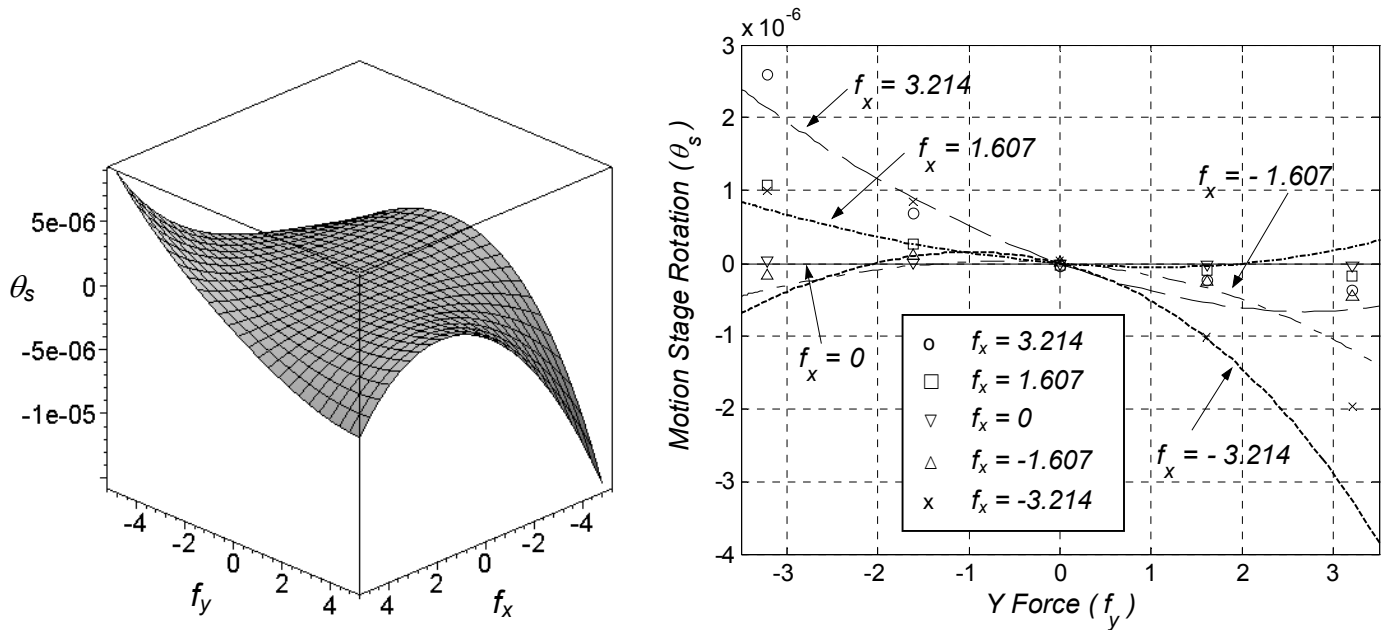
Fig.19 Motion Stage Rotation: CFA (Contour), CFA (Lines) and FEA (Marks)

Expression (26) also provides a quantitative assessment of the sensitivity of the stage rotation with respect to offsets e_x and e_y in the actuation axis, by setting $m_x = f_x\,e_x$ and $m_y = f_y\,e_y$. This is two times better than the previous design for small loads, and four times better for higher loads. The specific case of $f_x = 0$ and $f_y = 3.214$ is plotted in Fig. 20, along with FEA results.

Fig.20 Moment Sensitivity and COS for the Stages with respect Y Force: CFA (–) and FEA (o)

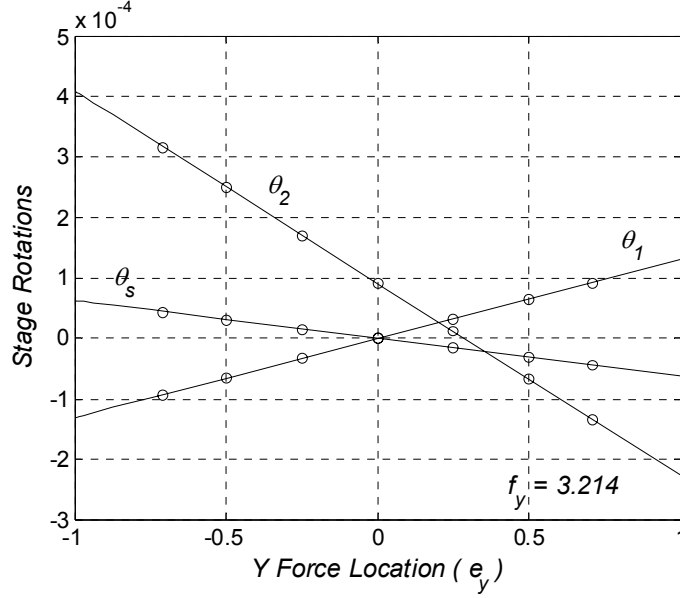Finally, we present the rotation of the intermediate stages assuming general loads but specific cases, to avoid complex expressions. For $\mathbf{f}_y = 0 = \mathbf{m}_y$,

$$\theta_1 = \left(\frac{64a^2 + rd\mathbf{f}_x^2}{128a^2 + rd\mathbf{f}_x^2}\right)\frac{\left[-rd\mathbf{f}_x^2\mathbf{m}_x + 32a^2\mathbf{f}_x(1+2a_o) - 320a^2\mathbf{m}_x\right]}{256a^2\overline{w}^2 d}$$

$$\theta_2 = \left(\frac{64a^2 + rd\mathbf{f}_x^2}{128a^2 + rd\mathbf{f}_x^2}\right)\frac{\left[a\mathbf{f}_x(b_o - 0.5) - \mathbf{m}_x a\right]}{4a\overline{w}^2 d} \qquad (27)$$

$$\theta_7 = \left(\frac{64a^2 + rd\mathbf{f}_x^2}{128a^2 + rd\mathbf{f}_x^2}\right)\frac{\left[rd\mathbf{f}_x^2\mathbf{m}_x + 32a^2\mathbf{f}_x(1+2a_o) + 64a^2\mathbf{m}_x\right]}{256a^2\overline{w}^2 d}$$

$$\theta_8 = \left(\frac{64a^2 + rd\mathbf{f}_x^2}{128a^2 + rd\mathbf{f}_x^2}\right)\frac{\left[a\mathbf{f}_x(b_o - 0.5) + \mathbf{m}_x a\right]}{4a\overline{w}^2 d}$$

These expressions provide the COS of the intermediate stages with respect to X actuation. Similarly, the intermediate stage rotations for $\mathbf{f}_x = 0 = \mathbf{m}_x$ are as follows, and provide the COS of the intermediate stages with respect to Y actuation.

$$\theta_1 = -\left(\frac{64a^2 + rd\mathbf{f}_y^2}{128a^2 + rd\mathbf{f}_y^2}\right)\frac{\left[a\mathbf{f}_y(b_o - 0.5) + \mathbf{m}_y a\right]}{4a\overline{w}^2 d}$$

$$\theta_2 = \left(\frac{64a^2 + rdf_y^2}{128a^2 + rdf_y^2} \right) \frac{\left[-rdf_y^2 m_y + 32a^2 f_y (1 + 2a_o) - 320a^2 m_y \right]}{256a^2 \overline{w}^2 d} \tag{28}$$

$$\theta_7 = \left(\frac{64a^2 + rdf_y^2}{128a^2 + rdf_y^2} \right) \frac{\left[-af_y (b_o - 0.5) + m_y a \right]}{4a\overline{w}^2 d}$$

$$\theta_8 = \left(\frac{64a^2 + rdf_y^2}{128a^2 + rdf_y^2} \right) \frac{\left[rdf_y^2 m_y + 32a^2 f_y (1 + 2a_o) + 64a^2 m_y \right]}{256a^2 \overline{w}^2 d}$$

The COS locations of the intermediate Stages 1 and 2 with respect to a Y actuation force are confirmed in Fig. 20. Assuming the forces are applied along the X_o and Y_o axes, rotations of the intermediate stages may be obtained by setting $m_x = m_y = 0$ in the above expressions. For the choice of $b_o = 1/2$, it is seen that Stage 1 and Stage 3 rotations can be made relatively insensitive to f_y, and Stage 2 and Stage 7 rotations can be made insensitive to f_x. Stages 1 and 2 rotations are plotted in Figures 21 and 22, respectively, for various loading conditions. The maximum rotation of any intermediate stage in this case is considerably less than the maximum Stage 2 rotation in the previous design.

While the tradeoffs between large range primary motion and other performance attributes remain, the symmetric constraint layout of this design yields much smaller motion stage and intermediate stage rotations, slightly better actuator isolation and reduced sensitivity to actuation force location. Although not explicitly derived, the out-of-plane characteristics of this design will also be considerably better owing to four anchor locations as opposed to just one.
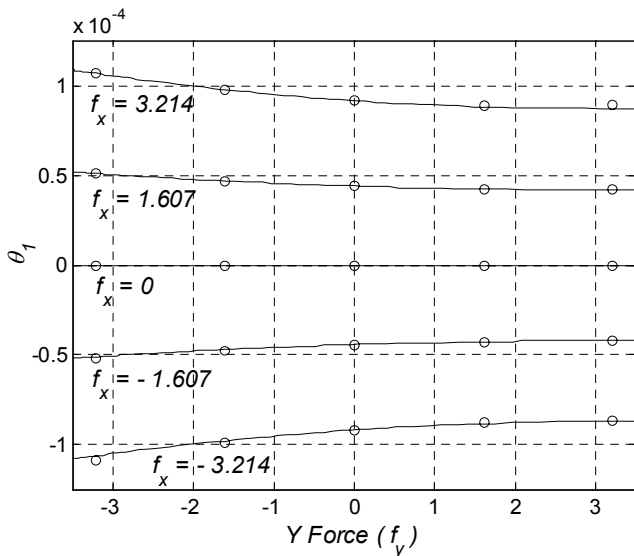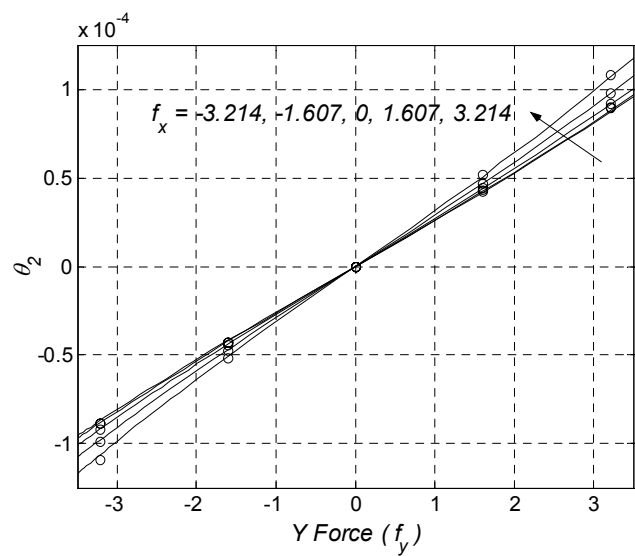

Fig.21 Stage 1 Rotation: CFA (–) and FEA (o)

Fig.22 Stage 2 Rotation: CFA (–) and FEA (o)

4. FEA and Experimental Results

A thorough Finite Element Analysis has been performed in ANSYS for both designs to validate the closed-form analysis (CFA) results. BEAM4 elements have been used with the large displacement option turned on and shear coefficients set to zero. The material assumed in both cases is AL6061 and the standard values for Young's Modulus ($69,000$ N.mm^{-2}) and Poisson's Ratio (0.3) are used. The characteristic beam length in both cases is 47.5mm, beam height is 25mm, and the remaining geometric parameters are listed below.

a_o	0.9737	r_o	0.9737	w_1	0.3882	t	$1/76$
b_o	0.5	s_o	0.9105	w_2	0.2697		

XY Mechanism Design 1

a_o	0.9737	s_x	1.3421	w_1	0.3882	t	$1/76$
b_o	0.5	s_y	1.1316	w_2	0.2697	r_o	0.9737

XY Mechanism Design 2

The geometric parameters for the two designs are kept identical or as close as possible to provide an even comparison. The closed-form analysis (CFA) and FEA predictions are found to be in close agreement. Significantly, the fairly complex and non-intuitive non-linear trends in the force-displacement relationships have been captured accurately and parametrically by the CFA. For Design 1, the difference between the predictions of the two analysis methods in terms of the primary motion, cross-axis error, lost motion, actuator isolation, motion stage rotation, and intermediate stage rotations is less than *0.5%, 15%, 4%, 2%, 2%*, and *0.5%*, respectively, over a primary motion range of ± *0.1*. For Design 2, except for the motion stage rotation, which is too small for a reasonable comparison, the remaining performance predictions using the CFA are within *0.3%, 4%, 4%, 1%*, and *7%*, respectively, of the FEA.

To experimentally verify these analytical predictions, an AL6061-T6 prototype of the XY Mechanism Design 2, with the above-mentioned dimensions, was fabricated using wire-EDM. The experimental set-up, shown in Fig. 23, has been designed such that the flexure stage can be actuated using free weights, motorized precision micrometers, and piezoelectric stacks. The metrology consists of plane-mirror laser interferometry, autocollimation and capacitance gages,

to characterize the translations and rotations of the motion stage and intermediate stages. Measurements were conducted on an isolation table, and corrected for temperature and humidity variations. Simultaneous measurements using multiple sensors and successive measurements using different actuators yield a reliable performance characterization. Measurement uncertainty is approximately *50*nm for displacements and *0.2*µrad for rotations.

The experimental measurements and analytical predictions for the XY Mechanism Design 2 displacements and rotations agree very well, as seen in Figures 15 through 18. The experiments yield an approximately *11%* higher primary motion stiffness, indicated in Fig. 15, as compared to the analysis. Since this stiffness comes primarily from the known transverse elastic stiffness coefficient of the simple beam, $a=12$, the observed discrepancy is most likely due to the assumed value of Young's Modulus. The experimental measurements also reveal a normalized elastic axial stiffness of the double parallelogram flexure modules that is *40%* less than the expected value, as evident from Fig. 17. This confirms that the axial stiffness of the beams, *d*, is not sufficient to capture the axial stiffness of the double parallelogram module if the secondary stage has a finite compliance [21]. The effect of the secondary stage compliance can be easily incorporated in the proposed analysis. The non-linear components of the cross-axis error motion and lost motion are measured to be within *5%* of the predicted values.
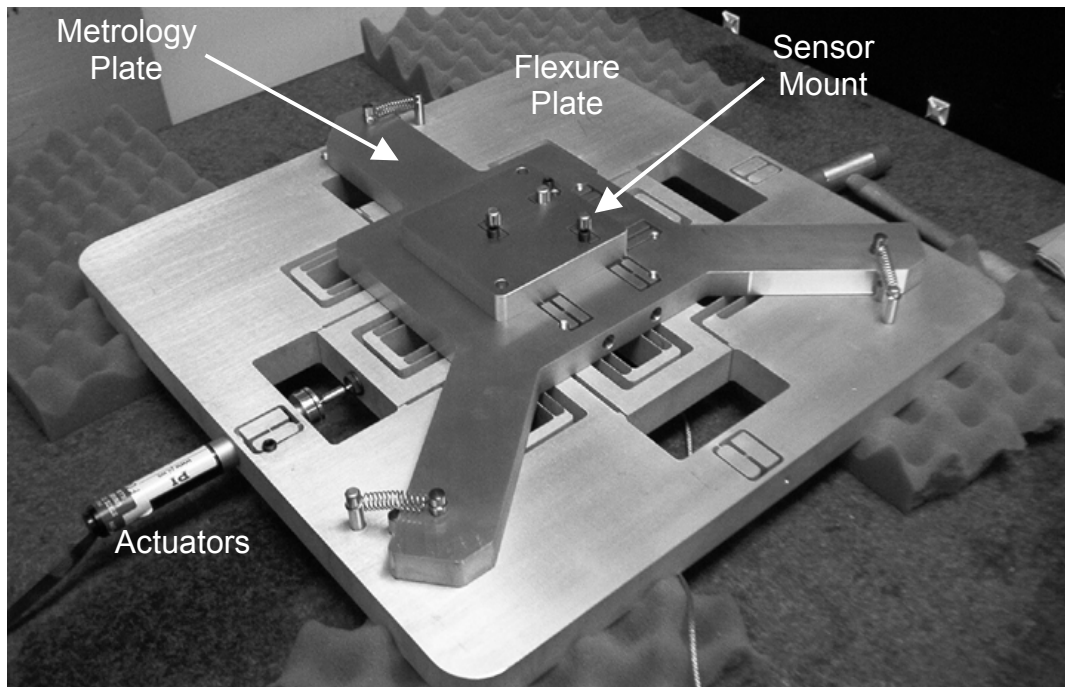

Fig.23 Experimental Set-up

5. Conclusion

There are three main contributions in this paper. Key performance attributes and challenges in XY mechanism design have been explained, and new parallel kinematic XY flexure mechanism designs based on systematic and symmetric constraint arrangements are proposed. These constraint arrangements allow large primary motions and small error motions without running into over-constraint problems. A *300*mm x *300*mm XY flexure stage with a motion range of *5*mm x *5*mm, cross-axis coupling, lost motion and actuator isolation better than *1%*, and a motion stage rotation of less than *1* arc sec, has been tested.

Second, this paper presents a parametric non-linear dimensionless analysis procedure for the performance prediction of beam-based flexure mechanisms. Based on simple yet accurate approximations for the beam and double parallelogram flexure force-displacement relations, it captures all the relevant non-linearities in the motion and force ranges of interest. Consequently, the relatively complex and non-intuitive non-linear trends in the force-displacement relationships of the proposed mechanisms have been derived to a high degree of accuracy. The nonlinear analysis reveals the importance of elastokinematic and load-stiffening effects, which are not captured by a linear analysis. This exposes the latter's inadequacy in performance evaluation over large motion ranges. The parametric nature of the analysis not only provides a better physical understanding of the mapping between the mechanism's geometry and performance, but also an ideal basis for shape and size optimization. The presented analysis is general in nature and remains valid for any beam shape variations.

Finally, we highlight the fact that there exist fundamental performance tradeoffs in flexure mechanism design, arising from the imperfect constraint properties of flexure elements. The closed-form force-displacement relationship predictions accurately quantify these performance attributes and tradeoffs. It is shown that the need to minimize cross-axis coupling, parasitic stage rotations, lost motion, and loss in actuator isolation and drive stiffness, conflicts with the desire for a large range of primary motion. These compromises depend on the characteristics of the individual building-block modules as well as the geometry of the layout. It is shown that Design 2, owing to its higher degree of symmetry, exhibits improved actuator isolation, lower stage rotations, and a higher degree of robustness against manufacturing and assembly errors, in comparison to Design 1. However, other performance attributes such as lost motion and drive

stiffness, being strongly dependent on the building-block characteristics, remain similar in nature and magnitude. It is also shown that the concept of Center of Stiffness may be used as a convenient means for the passive minimization of stage rotations. However, the effectiveness of this method is influenced by the mechanism's geometry, with the symmetric design proving to be a more suitable candidate.

Several avenues for future work are currently being pursued. The compliance of the secondary stage in the double parallelogram flexure modules can easily by modeled and included in the closed-form analysis to obtain more accurate and realistic performance predictions. Since certain performance attributes may not be improved simply by a symmetric geometry of constraint arrangement, other building blocks may be considered depending upon the requirements of a given application. For motion stages designed for high dynamic performance, the elastokinematic drive stiffness can be considerably improved by the use of the double tilted-beam flexure module [12], which preserves axial stiffness but is detrimental to parasitic stage rotations. Furthermore, beam shape optimization allows for the fine-tuning of the beam characteristic coefficients to achieve specific improvements in the performance attributes.

To facilitate the nonlinear analysis, we are developing a symbolic computation tool in MAPLE^{TM} that would allow a quick performance evaluation of any 2-D beam-based flexure design concept. It may be noticed that the system equations have been explicitly solved to arrive at the force-displacement results. The use of energy methods can prove to be tricky in problems with elastokinematic non-linearities and is currently being explored in order to make the analysis more efficient. The elastokinematic and load-stiffening effects lead to stiffness variations and couplings between displacement coordinates, thereby significantly affecting the dynamic characteristics of the proposed designs. An accurate dynamic model of the mechanisms that incorporates these effects is necessary for the design of a high-precision high-bandwidth motion system, and is being developed. For high-precision applications, the determination of thermal sensitivity is also a key requirement and may be incorporated within the proposed analysis framework.

References

1. Ryu, J.W., Gweon, D.-G., and Moon, K.S., 1997, "Optimal Design of a Flexure Hinge based X-Y-θ Wafer Stage", Journal of Precision Engineering, **21**(1), pp. 18-28.

2. Smith, A.R., Gwo, S., and Shih, C.K. 1994, "A New High Resolution Two-dimensional Micropositioning Device for Scanning Probe Microscopy", Review of Scientific Instruments, **64** (10), pp. 3216-3219.

3. Eom, T.B. and Kim, J.Y., 2001, "Long Range Stage for the Metrological Atomic Force Microscope", *Proc. ASPE 2001 Annual Meeting*, pp. 156-159.

4. Gorman, J. J. and Dagalakis, N. G., 2003, "Force control of linear motor stages for microassembly", IMECE2003-42079, *ASME International Mechanical Engineering Conference and Exposition*, Washington, DC.

5. Vettiger, P., et al., 2000, "The Millipede − More than one thousand tips for future AFM data storage", IBM Journal of Research and Development, **44** (3), pp. 323-340.

6. ADXL Accelerometers and ADXRS Gyroscopes, www.analogdevices.com

7. Agilent Nanostepper J7220, www.labs.agilent.com

8. XY Nanopositioner P-733, www.physikinstrumente.com

9. Chang, S.H., Tseng, C.K., and Chien, H.C., 1999, "An Ultra-Precision $XY\theta_Z$ Piezo-Micropositioner Part I: Design and Analysis", IEEE Transactions on Ultrasonics, Ferroelectrics, and Frequency Control, **46** (4), pp. 897-905.

10. Chen, K.S., Trumper, D.L., and Smith, S.T., 2002, "Design and Control for an Electromagnetically driven X-Y-θ Stage", Journal of Precision Engineering and Nanotechnology, **26**, pp. 355-369.

11. Awtar, S., 2004, "Analysis and Synthesis of Planer Kinematic XY Mechanisms", Sc.D. thesis, Massachusetts Institute of Technology, Cambridge, MA. (http://web.mit.edu/shorya/www)

12. Awtar, S. and Slocum, A.H., 2005, "Closed-form Nonlinear Analysis of Beam-based Flexure Modules", *Proc. ASME IDETC/CIE 2005*, Long Beach, CA, Paper No. 85440

13. Ananthasuresh, G.K., Kota S., and Gianchandani, Y., 1994, "A Methodical Approach to Design of Compliant Micromechanisms", *Solid State Sensor and Actuator Workshop*, Hilton Head Island, SC, pp. 189-192.

14. Frecker, M.I., Ananthasuresh, G.K., Nishiwaki, S., Kickuchi, N., and Kota S., 1997, "Topological Synthesis of Compliant Mechanisms Using Multi-criteria optimization," Journal of Mechanical Design, **119**, pp. 238-245.

15. Blanding, D.K., 1999, *Exact Constraint: Machine Design Using Kinematic Principles*, ASME Press, New York, NY.

16. Awtar S., and Slocum A.H., 2004, "Apparatus Having motion with Pre-determined degree of Freedom", US Patent 6,688,183 B2.

17. Bisshopp, K.E., and Drucker, D.C., 1945, "Large Deflection of Cantilever Beams", Quarterly of Applied Mathematics, **3** (3), pp. 272-275.

18. Howell L.L, 2001, *Compliant Mechanisms*, John Wiley & Sons, New York, NY.

19. Plainevaux, J.E., 1956, "Etude des deformations d'une lame de suspension elastique", Nuovo Cimento, **4**, pp. 922-928.

20. Legtenberg, R., Groeneveld, A.W. and Elwenspoek, M., 1996, "Comb-drive Actuators for Large Displacements", Journal of Micromechanics and Microengineering, **6**, pp. 320-329.

21. Saggere, L., Kota, S., 1994, "A New Design for Suspension of Linear Microactuators", ASME Journal of Dynamic Systems and Control, **55** (2), pp. 671-675.

List of Figure Captions

Fig.1   Proposed Constraint Arrangement for XY Flexure Mechanisms

Fig.2   XY Flexure Mechanism Design 1

Fig.3   XY Flexure Mechanism Design 2

Fig.4   Double Parallelogram Flexure Module

Fig.5   XY Mechanism 1 in a Deformed Configuration

Fig.6   Primary Motion: CFA (–) and FEA (o)

Fig.7   Cross-Axis Error Motion: CFA (–) and FEA (o)

Fig.8   Lost Motion / Drive Stiffness: CFA (–) and FEA (o)

Fig.9   Actuator Isolation: CFA (–) and FEA (o)

Fig.10   Motion Stage Rotation: CFA (Contour), CFA (–) and FEA (o)

Fig.11   Moment Sensitivity and COS for the Stages with respect X Force: CFA (–) and FEA (o)

Fig.12   Stage 1 Rotation: CFA (–) and FEA (o)

Fig.13   Stage 2 Rotation: CFA (–) and FEA (o)

Fig.14   XY Mechanism 2 in a Deformed Configuration

Fig.15   Primary Motion: CFA (–), FEA (o), Exp (*)

Fig.16   Cross-axis Error Motion: CFA (–), FEA (o), Exp (*)

Fig.17   Lost Motion / Drive Stiffness: CFA (–), FEA (o), Exp (*)

Fig. 18   Actuator Isolation: CFA (–), FEA (o), Exp (*)

Fig.19   Motion Stage Rotation: CFA (Contour), CFA (Lines) and FEA (Marks)

Fig.20   Moment Sensitivity and COS for the Stages with respect Y Force: CFA (–) and FEA (o)

Fig.21   Stage 1 Rotation: CFA (–) and FEA (o)

Fig.22   Stage 2 Rotation: CFA (–) and FEA (o)

Fig.23   Experimental Set-up